

PAPER • OPEN ACCESS

Ferroelectric semiconductor junctions based on graphene/In₂Se₃/graphene van der Waals heterostructures

To cite this article: Shihong Xie *et al* 2021 *2D Mater.* **8** 045020

View the [article online](#) for updates and enhancements.



PAPER

OPEN ACCESS

RECEIVED
29 April 2021REVISED
19 July 2021ACCEPTED FOR PUBLICATION
4 August 2021PUBLISHED
20 August 2021

Original content from this work may be used under the terms of the [Creative Commons Attribution 4.0 licence](#).

Any further distribution of this work must maintain attribution to the author(s) and the title of the work, journal citation and DOI.



Ferroelectric semiconductor junctions based on graphene/In₂Se₃/graphene van der Waals heterostructures

Shihong Xie^{1,2} , Anubhab Dey¹, Wenjing Yan¹, Zakhar R Kudrynskiy¹ , Nilanthy Balakrishnan^{3,4} , Oleg Makarovskiy¹, Zakhar D Kovalyuk⁵, Eli G Castanon⁶, Oleg Kolosov⁶ , Kaiyou Wang² and Amalia Patane^{1,*}

¹ School of Physics and Astronomy, University of Nottingham, NG7 2RD Nottingham, United Kingdom

² State Key Laboratory of Superlattices and Microstructures, Institute of Semiconductors, Chinese Academy of Sciences, Beijing 100083, People's Republic of China

³ School of Chemical and Physical Sciences, Keele University, ST5 5BG Keele, United Kingdom

⁴ National Graphene Institute, The University of Manchester, M13 9PL Manchester, United Kingdom

⁵ Frantsevich Institute for Problems of Materials Science, The National Academy of Sciences of Ukraine, Chernivtsi Branch, 58001 Chernivtsi, Ukraine

⁶ Department of Physics, Lancaster University, LA1 4YB Lancaster, United Kingdom

* Author to whom any correspondence should be addressed.

E-mail: amalia.patane@nottingham.ac.uk

Keywords: ferroelectrics, semiconductors, two-dimensional materials, electron transport, photoresponse

Supplementary material for this article is available [online](#)

Abstract

The miniaturization of ferroelectric devices offers prospects for non-volatile memories, low-power electrical switches and emerging technologies beyond existing Si-based integrated circuits. An emerging class of ferroelectrics is based on van der Waals (vdW) two-dimensional materials with potential for nano-ferroelectrics. Here, we report on ferroelectric semiconductor junctions (FSJs) in which the ferroelectric vdW semiconductor α -In₂Se₃ is embedded between two single-layer graphene electrodes. In these two-terminal devices, the ferroelectric polarization of the nanometre-thick In₂Se₃ layer modulates the transmission of electrons across the graphene/In₂Se₃ interface, leading to memristive effects that are controlled by applied voltages and/or by light. The underlying mechanisms of conduction are examined over a range of temperatures and under light excitation revealing thermionic injection, tunnelling and trap-assisted transport. These findings are relevant to future developments of FSJs whose geometry is well suited to miniaturization and low-power electronics, offering opportunities to expand functionalities of ferroelectrics by design of the vdW heterostructure.

1. Introduction

Since the pioneering studies in the 1920s by Joseph Valasek on ferroelectricity in Rochelle salt (e.g. KNaC₄H₄O₆·4H₂O) [1], ferroelectric materials have had an enormous impact in science and exploited in many technologies ranging from high-energy capacitors and transducers to ultrasound medical imaging [2–4]. More recently, the observation of ferroelectricity in van der Waals (vdW) crystals has attracted significant interest [5–8]. These two-dimensional (2D) layered materials can exhibit ferroelectricity above room temperature and for layer thicknesses down to a few layers of atoms. Their implementation in miniaturized devices could open paths towards multifunctional sensors for

digital technologies, nano-electromechanical systems, increased storage capacity of non-volatile memories, neuromorphic computing, etc [9–12]. For example, resistance switching by ferroelectricity could be exploited in nanoscale memristive devices (or memristors) to store and process information for non-volatile, low-power electrical switches [13]. Thus, understanding the limitations and potential of this emerging class of 2D ferroelectrics is important for future scientific and technological advances.

In a ferroelectric material, the crystal lattice is polarized along a specific direction, generating a macroscopic electrical polarization **P** that can be reversed by an applied electric field **E**. The electric polarization arises from a structural asymmetry of the crystal along the direction of the polarization leading

to a nonlinear dependence of the polarization amplitude P on the strength of the electric field, E , and an S-shaped hysteresis loop in the P - E curve [3]. For atomically thin layers, the ferroelectric state can be difficult to detect due to a weak polarization signal; it may require a large applied electric field to be reversed, leading to electrical breakdown; finite-size effects, such as depolarization fields at interfaces, can destabilize the ferroelectric polarization [14, 15]; furthermore, localization of charge carriers onto defects, crystalline phase changes and/or electrochemical processes can influence ferroelectric properties and device performance [16, 17].

Amongst 2D ferroelectrics, the vdW semiconductor α - In_2Se_3 has emerged as a promising material due to its room temperature in-plane (IP) and out-of-plane (OOP) ferroelectricity [15, 18–20] and a low coercive electric field ($\sim 10^7 \text{ V m}^{-1}$) [20]. Its use in 2D ferroelectric devices has been reported and includes ferroelectric field effect transistors (FeFETs) with the ferroelectric semiconductor serving as conducting channel [11, 16, 19, 21] or dielectric gate [9, 22], and ferroelectric semiconductor junctions (FSJs) based on a thin α - In_2Se_3 layer embedded between single-layer graphene and few layer graphene electrodes [20]. The geometry of the FSJ is well suited to miniaturization and low-power applications. Furthermore, the conductivity properties of a ferroelectric semiconductor can be modified by temperature and light, providing broad prospects for applications of ferroelectric devices.

Here, we report on FSJs based on the ferroelectric vdW semiconductor α - In_2Se_3 embedded between two single-layer graphene electrodes (figure 1(a)). In the FSJ, the polarization of the nanometre-thick In_2Se_3 layer is controlled by a voltage applied between two graphene electrodes, thus modifying the Schottky-like barrier at the graphene/ In_2Se_3 interface [15, 20]: the change in the height of the barrier modulates the transmission of electrons across the interface, leading to memristive effects. We show that this is a robust process over a wide range of temperatures, below and above room temperature. Also, it can be modified by a relatively small applied voltage ($\sim 1 \text{ V}$) and by light: the free carriers generated by light and/or thermionic injection can neutralize the polarization charges at the graphene/ α - In_2Se_3 interface and influence the hysteretic behaviour in the electrical transport, offering opportunities for future developments.

2. Results and discussion

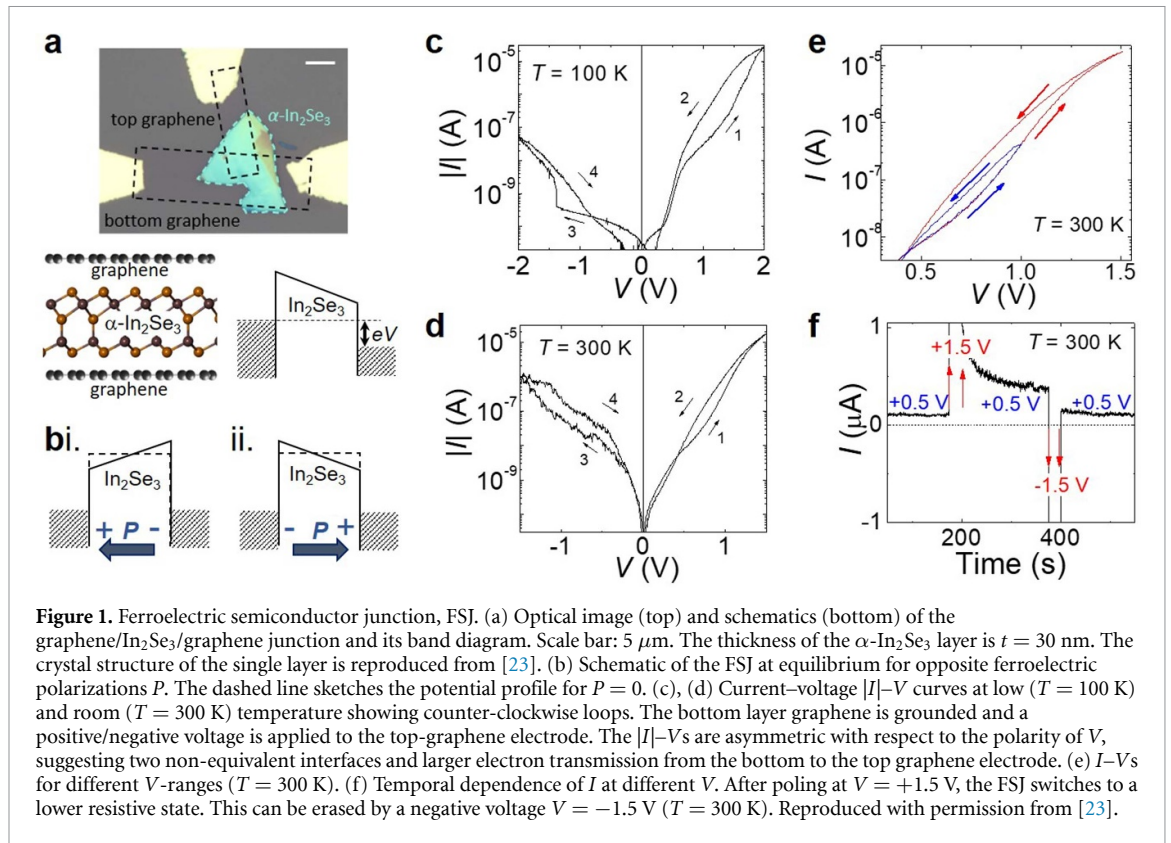
2.1. FSJs

For our studies we focus on the α -phase of In_2Se_3 , which is ferroelectric at room temperature with a Curie temperature T_c above 500 K [18]. The preliminary characterization of the α - In_2Se_3 crystals by x-ray diffraction, piezoresponse force microscopy

(PFM), Raman and photoluminescence (PL) spectroscopy is in the Methods section and in figures S1 and S2 (available online at stacks.iop.org/2DM/8/045020/mmedia) of supplementary material S1. Amongst the different crystalline phases of In_2Se_3 , the α -phase exhibits either a rhombohedral (3R) or a hexagonal (2H) crystal structure [6, 23]. For both structures, the single vdW In_2Se_3 layer consists of five atomic layers stacked in the sequence Se–In–Se–In–Se (one quintuplet layer, QL), which exhibits reversible spontaneous electric polarization in both OOP and IP orientations [15, 18–20]. The asymmetric position of the Se-atoms inside each QL breaks the centro-symmetry of the crystal, providing two degenerate energy states with opposite OOP polarization and IP asymmetry. To reverse the OOP polarization, the middle Se-atom must move along the c -axis and in the ab -plane, leading to a break up and reconfiguration of the In–Se covalent bond [15, 21]. The OOP polarization of α - In_2Se_3 is important for miniaturization of electrical components that require vertical device architectures, such as the FSJ.

Our graphene/ In_2Se_3 /graphene vdW heterostructures are assembled by exfoliation and mechanical stamping of nanometre-thick vdW layers (see section 4). The optical image and schematics of the band alignments for a FSJ with a 30 nm thick α - In_2Se_3 layer are illustrated in figures 1(a) and (b). Under a voltage applied between the two graphene electrodes of the FSJ, electrons are injected from the negatively biased graphene electrode onto the α - In_2Se_3 layer and collected at the second graphene electrode (figure 1(a)). For an electric field larger than the coercive field, the ferroelectric layer becomes polarized and the polarized charges at the graphene/ α - In_2Se_3 interface shift the Dirac cone of graphene relative to the conduction band (CB) of α - In_2Se_3 , thus lowering (figure 1(b), (i)) or increasing (figure 1(b), (ii)) the potential barrier seen by electrons. The polarization charges decrease the potential barrier at one interface, while they increase it at the other interface. Also, the applied voltage creates an asymmetry in the junction so that the interface between the negatively biased graphene electrode and the α - In_2Se_3 barrier dominates: once electrons are injected across the first interface, they travel throughout the ferroelectric layer reaching the second interface with graphene where there are available empty states (figure 1(a)). For an electric field larger than the coercive field, the potential barrier seen by the electrons at the first interface decreases. This leads to an increased transmission of electrons throughout the device, causing resistance switching and memristive behaviours.

The current–voltage $|I|$ - V curves of the FSJ reveal counter-clockwise loops at $T = 100 \text{ K}$ (figure 1(c)) and $T = 300 \text{ K}$ (figure 1(d)): the amplitude of the current is larger when sweeping the voltage from high to low positive V (or from high to low negative V). The applied voltage is critical to the observation



of the hysteretic behaviour in I – V . As shown in figure 1(e), the counter-clockwise loop becomes more pronounced at larger V . Weaker clockwise loops are instead observed at low V . For the device of figure 1, a voltage $|V| = 1\ \text{V}$ corresponds to an electric field $E = |V|/t > 0.3 \times 10^8\ \text{V m}^{-1}$, where $t \approx 30\ \text{nm}$ is the thickness of the α - In_2Se_3 layer.

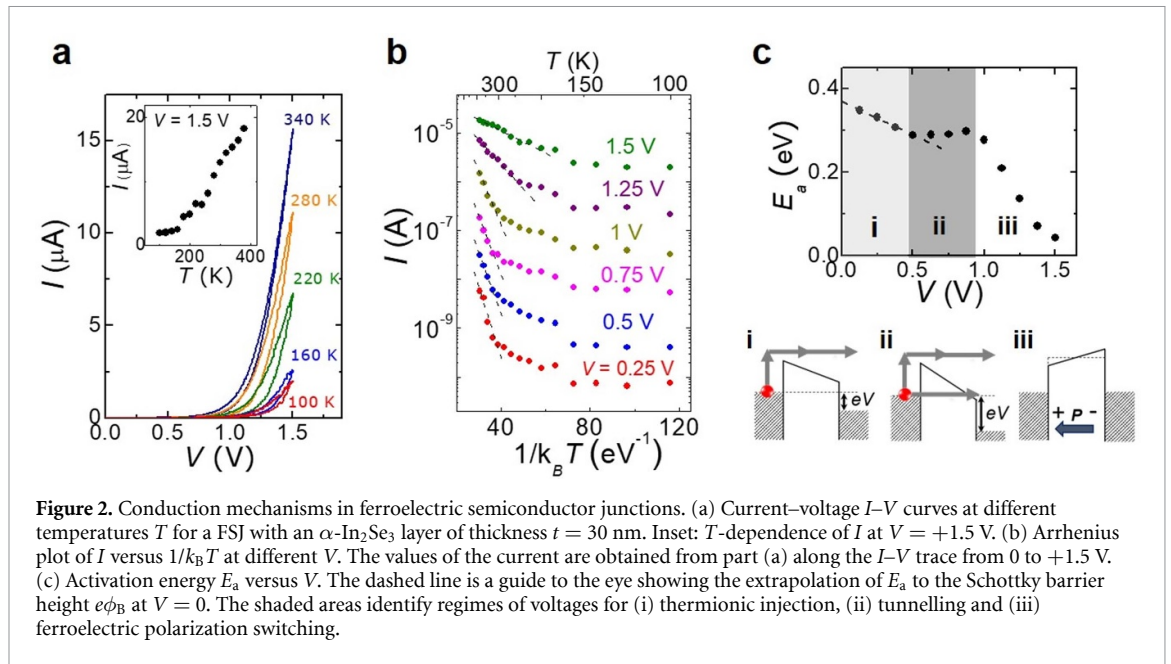
The transport properties of the FSJ are further probed by monitoring the temporal dependence of the current under different applied voltages and electric poling conditions of the FSJ. The current measured at a low bias ($V = +0.5\ \text{V}$) takes different values following a poling of the FSJ at a larger positive or negative voltage (see figure 1(f) for poling at $V = +1.5\ \text{V}$). The initial resistive state can be resumed by applying a negative (or positive) bias after poling at $V > 0$ (or $V < 0$) (figure 1(f)). Similar counter-clockwise loops in I – V and memristive effects were observed in FSJs with different thicknesses of the α - In_2Se_3 layer (figure S3 in supplementary material S2). In contrast, they are not observed in FETs based on long ($>1\ \mu\text{m}$) α - In_2Se_3 channels, whose electrical properties and hysteretic behaviours are dominated by charge injection onto trap sites (supplementary material S3).

A large electric field is required to induce a ferroelectric polarization in α - In_2Se_3 by displacements of the In- and Se-atoms within each vdW layer. PFM demonstrates switching of the polarization at the nanoscale and possibility to create local stable OOP domains (figure S2 in supplementary material S1). The calculated amplitude of the electric dipoles

is 0.11 and 0.03 $\text{e}\text{\AA}$ per α - In_2Se_3 unit cell for the two oppositely polarized configurations, influencing the atomic orbitals and energy band alignments at the graphene/ α - In_2Se_3 interface [15]: the chemical potential in graphene moves upward or downward according to the sign of the polarization charges so that more or fewer electrons can transverse the junction. At low T (figure 1(c)), the steeper increase of the current at $|V| > 1\ \text{V}$ suggests a switchable polarization of the ferroelectric layer, thus increasing the current throughout the junction; this behaviour is also observed at room temperature, but it is less pronounced (figure 1(d)).

2.2. Thermionic injection and tunnelling

We probe the mechanisms of conduction in the FSJ and the robustness of the memristive behaviour against a rising temperature by considering the I – V s over a range of temperatures from $T = 100\ \text{K}$ to $T = 380\ \text{K}$. As shown in figure 2(a), the counter-clockwise loop in I – V persists above $T = 300\ \text{K}$, although is significantly reduced at $T = 340\ \text{K}$. For $T < 150\ \text{K}$, the current and hysteretic behaviours are weakly dependent on T ; in contrast, at higher temperatures, the current tends to increase exponentially with T , following a dependence described by $I \sim \exp(-E_a/k_B T)$, where k_B is the Boltzmann constant and E_a is an activation energy (figure 2(b)). From the Arrhenius plots of figure 2(b), we extract the value of E_a and its dependence on V (figure 2(c)): with increasing V , E_a first decreases, reaches a



constant value between $V \sim 0.5$ V and $V \sim 1$ V, and then it decreases for $V > 1$ V.

The temperature dependence of the current suggests a contribution to the transport from thermionic injection of electrons from the graphene electrode onto the CB of α - In_2Se_3 (figure 2(c), (i)). For thermionic injection, the emission current density can be described as $J = J_s[\exp(qV/k_B T) - 1]$ [24], where $J_s = A^* T^2 \exp(-q\phi_B/k_B T)$, A^* is the effective Richardson constant, $q = e$ is the elementary electron charge, and $q\phi_B$ is the Schottky barrier height at the graphene/semiconductor interface. The current is thermally activated with an activation energy E_a that increases with decreasing V extrapolating to $q\phi_B$ at $V = 0$ V. As shown in figure 2(c), our FSJs reveal this dependence at low V with $E_a = q\phi_B = (0.38 \pm 0.01)$ eV at $V = 0$. From the measured position of the Fermi level, E_F , in our p -type graphene electrode at $V = 0$, we deduce that the neutral Dirac point of graphene lies at $\Delta E = q\phi_B - E_F \approx 0.25$ eV below the CB edge of α - In_2Se_3 at $V = 0$ V (supplementary material S1).

The Schottky barrier model is in agreement with that expected from density functional theory for a graphene/ α - In_2Se_3 interface [15]. However, the graphene/ α - In_2Se_3 interface does not behave as a simple Schottky contact. The constant value of E_a with increasing V from $V \sim +0.5$ V to $V = +1$ V followed by a steep decrease for $V > +1$ V (figure 2(c)) cannot be explained by thermionic injection. On the other hand, under a large applied electrical field, electrons can tunnel from the electrode onto the CB of α - In_2Se_3 through a triangular potential barrier (Fowler–Nordheim tunnelling, figure 2(c), (ii)), causing a weaker dependence of the current on temperature than for thermionic injection. Furthermore, as the voltage increases beyond the coercive field,

the polarization charges at the graphene/ α - In_2Se_3 interface induce an effective lowering of the Schottky barrier (figure 2(c), (iii)). This can account for the decrease of E_a at high V and the corresponding increase of conduction in the low-resistive ferroelectric state of the FSJ. In summary, the modulation of the graphene/ α - In_2Se_3 interface by polarization switching can be modelled as a tuneable Schottky barrier: a change in the height of the barrier modulates the transmission of electrons across the FSJ. At low T (< 150 K) charge injection is dominated by tunnelling, whereas thermal injection becomes more prominent as the temperature increases above $T = 150$ K. The reduced memristive effects with increasing T arise from the increased current in the FSJ acting to diminish the polarization of α - In_2Se_3 .

We have examined FSJs with different layer thickness (see figures S3 and S4 in supplementary material S2). All structures show similar hysteretic behaviours in the electrical transport. Although the transmission of electrons by direct tunnelling is reduced in thicker layers, trap-assisted tunnelling can dominate at high applied voltages. Under a large applied electrical field, the conduction electrons in the α - In_2Se_3 layer can acquire sufficient energy to ionize charge trap sites, generating additional electrons by inelastic collisions. Electron emission from traps is also influenced by the electric field due to Poole–Frenkel emission [25]. Carrier traps can arise from In-vacancies and/or residual n -type dopants that reside in the interlayer gaps of α - In_2Se_3 [26]. Their existence is supported by Hall effect measurements of bulk α - In_2Se_3 , giving a Hall electron density of up to $n = 4.9 \times 10^{17} \text{ cm}^{-3}$ at $T = 300$ K (see Methods sections and figures S3 and S4 in supplementary material S2). The ionization of impurities and/or defects at high electric fields and/or temperature is pivotal to the operation of FSJs,

requiring optimization of the doping properties of the ferroelectric semiconductor. We note that the thermal excitation of electrons from the valence band to the CB of α -In₂Se₃ creates free carriers whose density depends on the band gap energy (E_g) and temperature ($E_g = 1.4$ eV at 300 K) (figure S1 in supporting materials S1). The thermal activation energy for this process is significantly larger than that derived from the thermally activated behaviour of the current in the FSJ (figure 2). Thus, we infer that the intrinsic thermal excitation of carriers can be neglected.

2.3. FSJs under light

Light provides a non-invasive method for switching ferroelectric properties and probe ferroelectrics [11, 27–30]: The built-in electric field due to the ferroelectric polarization can induce photovoltaic effects [27, 28] and modify the ferroelectric polarization by screening of polarization charges [30]. Here, we examine light-polarization interactions in our FSJs using laser light of energy $h\nu = 1.96$ eV ($\lambda = 633$ nm) above the band gap of α -In₂Se₃ ($E_g = 1.4$ eV at 300 K) (figure S1 in supporting materials S1). In these experiments the FSJ is illuminated through the transparent top graphene electrode.

As shown in figure 3, an increasing laser power P_i induces a positive photocurrent ΔI and reduces the hysteretic loops in I - V . We examine the photoresponse of the FSJ by considering the dependence of the photoresponsivity, $R = \Delta I/P_i$, on V and P_i for two FSJs with different layer thicknesses ($t = 30$ and 200 nm in figures 4(a)–(c) and (b)–(d), respectively). As can be seen in figure 4, for both FSJs R increases by several orders of magnitude with increasing V and is larger at low powers.

At first glance, the photoresponse of the FSJ can be understood by considering the dynamics of photocreated carriers (figure 4(e)). Under an applied voltage V , electrons and holes that are photoexcited in the α -In₂Se₃ layer are swept by the electric field in opposite directions and extracted at the graphene electrodes (figure 4(e), (i)) to generate a photocurrent $\Delta I = [q\alpha P_i/h\nu]\tau_1/\tau_t$, where α is the absorption coefficient of α -In₂Se₃ at the photon energy $h\nu$, t is the thickness of the α -In₂Se₃ layer, and τ_1/τ_t is the ratio of the minority carrier lifetime (τ_1) to the transit time (τ_t) of majority carriers in α -In₂Se₃. In these FSJs, the majority carriers are electrons due to residual n -type doping of α -In₂Se₃ ($n = 4.9 \times 10^{17}$ cm⁻³ at $T = 300$ K). Thus, we express R as $R = \Delta I/P_i = [e\alpha/h\nu]\tau_1/\tau_t$ and the external and internal quantum efficiencies as $\text{EQE} = R(h\nu/e) = [t\alpha]\tau_1/\tau_t$ and $\text{IQE} = \tau_1/\tau_t$, respectively. These relations indicate that large values of R , EQE and IQE are achieved if the lifetime of holes is longer than the transit time of electrons.

As shown in figures 4(c) and (d), R follows a power dependence described by P_i^β with $\beta = -0.48 \pm 0.02$ for $t = 30$ nm and

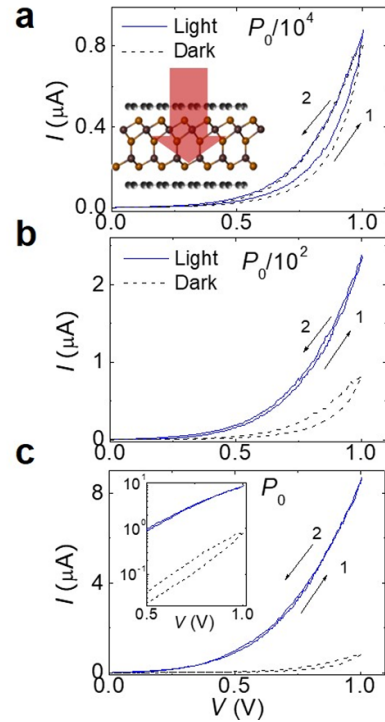


Figure 3. Ferroelectric semiconductor junctions under light. Current–voltage I - V in the dark (black) and under laser light (blue) of energy $h\nu = 1.96$ eV ($\lambda = 633$ nm) and power (a) $P_0/10^4$, (b) $P_0/10^2$, and (c) P_0 for a FSJ with $t = 30$ nm ($T = 300$ K, $P_0 = 10^{-8}$ W). Inset, top panel: illumination of the FSJ from the top graphene electrode. Inset, bottom panel: I - V s with and without light.

$\beta = -0.71 \pm 0.03$ for $t = 200$ nm. The largest values of R (up to $R = 10^6$ A W⁻¹) are reached for low $P_i = 10^{-12}$ W. For $t = 30$ nm, $V = +1$ V and $\alpha = 10^6$ m⁻¹ at $h\nu = 1.96$ eV, we estimate that τ_1/τ_t decreases from $\sim 2 \times 10^6$ to $\sim 2 \times 10^4$ with P_i going from 10^{-12} W to $\sim 10^{-8}$ W. A value of $\tau_1/\tau_t = 2 \times 10^6$ corresponds to a large internal gain with $\text{IQE} = 2 \times 10^6$, $\text{EQE} = R[h\nu/e] = 7 \times 10^4$ and $D^* = R(A/2eI)^{1/2} \sim 5 \times 10^{11}$ m W⁻¹ s^{-1/2}, where $A = 20$ μm^2 is the area of the device and $I = 0.8$ μA is the dark current at $V = +1$ V.

The decrease of R , EQE and D^* with increasing P_i is similar to that reported for other 2D materials [31–35] and can be accounted for by the decrease of τ_1/τ_t with increasing P_i due to either a decrease of τ_1 and/or an increase of τ_t with increasing P_i . The transit time of majority electrons can increase with P_i due to enhanced carrier scattering. The lifetime of minority holes is limited by Shockley–Read and surface recombination and is reduced at high carrier densities (or high P_i) due to Auger recombination [24]. The dependence of R on P_i is more pronounced in the thicker FSJs, suggesting a stronger contribution from trap-assisted carrier recombination (figure 4(e), (ii)). All our FSJs reveal a similar high, fast temporal photoresponse. Figure 5(a) shows the temporal dependence of the current under illumination of an

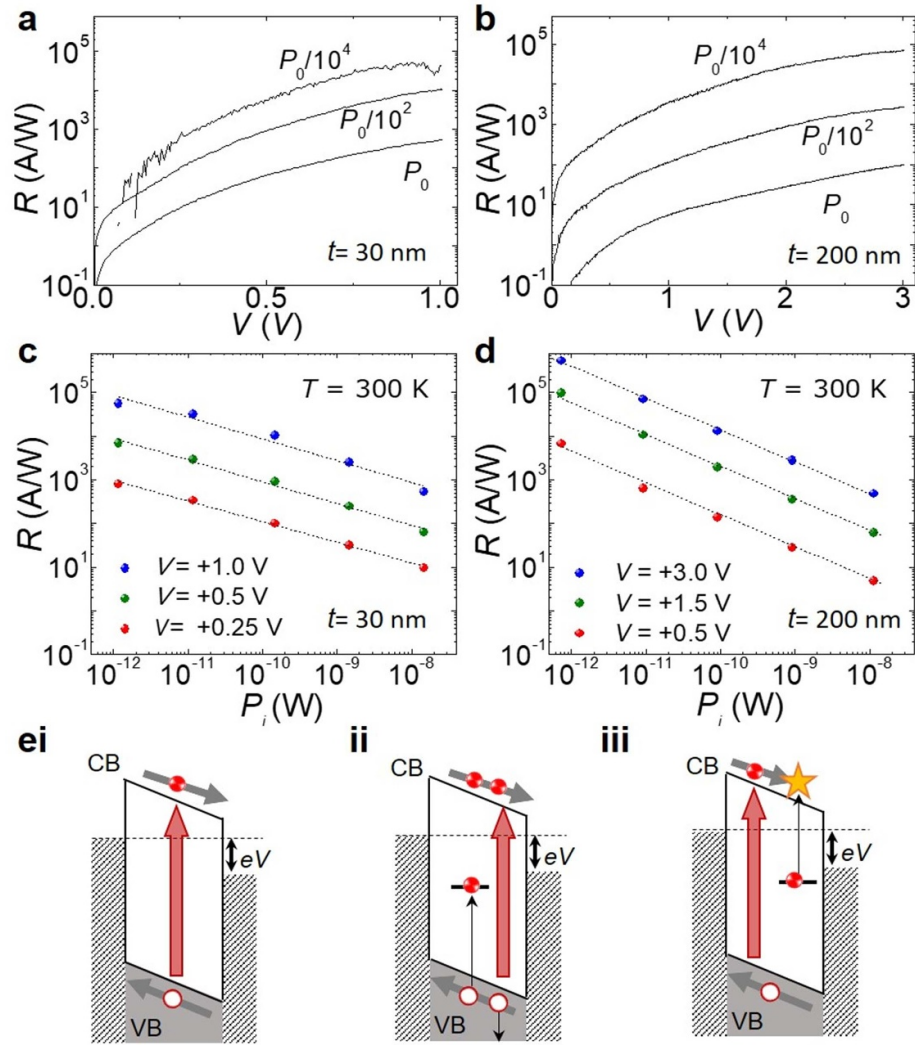


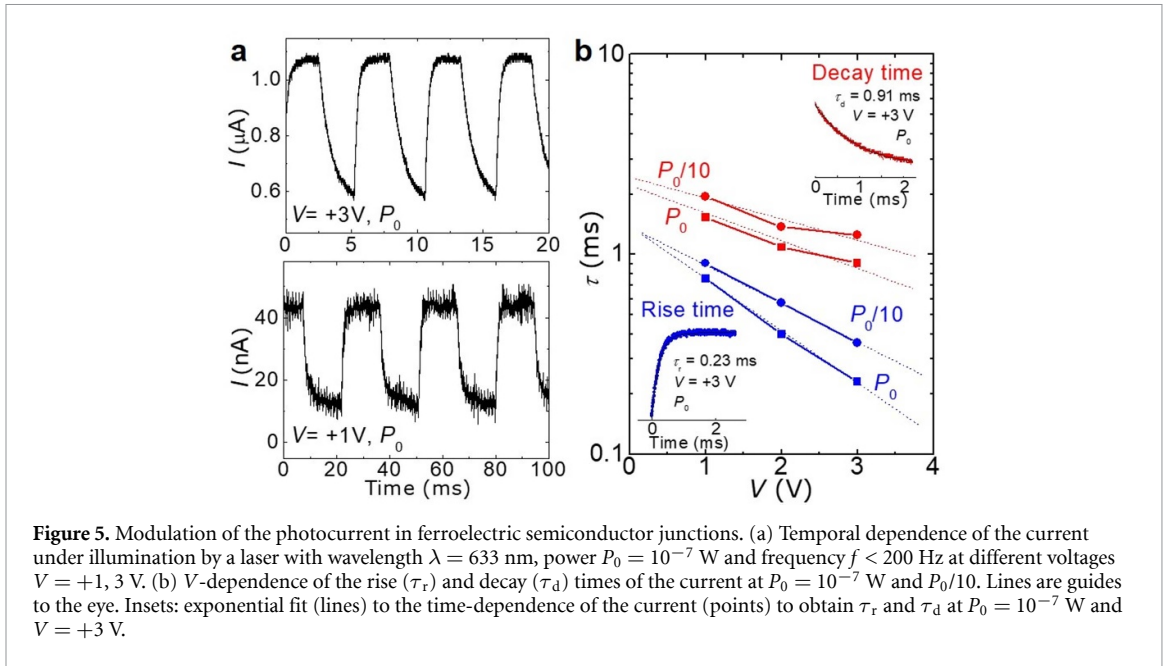
Figure 4. Photoresponsivity of ferroelectric semiconductor junctions. (a), (b) Photoresponsivity (R) versus voltage (V) at different powers P_i for laser light of energy $h\nu = 1.96$ eV ($\lambda = 633$ nm) and FSJs with $t = 30$ nm (a) and 200 nm (b) ($T = 300$ K). (c), (d) R versus P_i for different V and FSJs with $t = 30$ nm (c) and 200 nm (d) ($T = 300$ K). Lines are fits to the data by a power dependence. (e) (i) Photogenerated electrons and holes and their separation by the electric field of the FSJ; (ii) capture of minority carriers (holes) by traps; (iii) impact ionization of traps.

FSJ with $t = 200$ nm (see also figure S6 in the supplementary material S5). The rise (τ_r) and decay (τ_d) times of the current are derived from an exponential fit to the data (figure 5(b)): they are both short (0.1–1 ms) with $\tau_d > \tau_r$ and both decreasing with increasing V and/or P_i .

We examine the data on photoresponsivity under different applied voltages and powers to examine the role of the ferroelectric polarization on the photoresponse of the FSJs. The photoresponsivity increases by several orders of magnitude with increasing V (figures 4(a) and (b)), reaching values comparable to or higher than those reported for other In_2Se_3 -based devices in the literature [31, 36–39]. The strong dependence of the photocurrent on V is also seen in tunnel junctions without the ferroelectric layer [34], suggesting that the ferroelectric polarization of the In_2Se_3 layer does not play a critical role in the high

values of R or in the dependence of R on V . The high photoresponsivity of the FSJ is primarily caused by a large internal gain and is not influenced by polarization charges at the graphene/ α - In_2Se_3 interface. On the other hand, photocreated carriers act to neutralize polarization charges, reducing the hysteresis loops in I – V (figure 3).

We assign the superlinear dependence of R on V to avalanche multiplication of carriers due to impact ionization of traps inside the band gap (figure 4(e), (iii)). This process can occur at lower fields than those required for band-to-band ionization as traps require a smaller ionization energy and their binding energy is reduced due to Poole–Frenkel effect [25]. For band-to-band impact ionization, the threshold energy for impact ionization, ε_{th} , should be larger than the band gap energy ($E_g = 1.4$ eV at 300 K for bulk crystals). A simple diffusive model of electron motion



indicates that the electric field required for an electron to acquire such energy ε_{th} would be larger than $E_{th} \sim 2.4 \times 10^9$ V m $^{-1}$, much larger than that considered in our experiments (supplementary material S4). On the other hand, an avalanche creation of free carriers by ionization of defects and/or impurities can occur for $E < E_{th}$.

3. Conclusions

In conclusion, the polarization of the ferroelectric vdW semiconductor α -In $_2$ Se $_3$ can be manipulated by applying a voltage across the two graphene electrodes of a graphene/ α -In $_2$ Se $_3$ /graphene junction. This acts to modify the Schottky barrier at the graphene/ α -In $_2$ Se $_3$ interface: a change in the height of the barrier modulates the transmission of electrons across the interface, leading to memristive effects. This is a robust process over a wide range of temperatures. However, it can be influenced by ionization of defects and impurities that reside in n -type α -In $_2$ Se $_3$, a phenomenon that tends to weaken the memristive effect. The additional free carriers generated by impact ionization, tunnelling and thermionic injection can neutralize the polarization charges at the graphene/ α -In $_2$ Se $_3$ interface and influence the hysteretic behaviour in the electrical transport. Light provides an effective route for modifying electronic properties and memristive effects. In particular, the FSJs reveal a high photoresponsivity and fast modulation of the photocurrent that exploit the optical absorption properties of α -In $_2$ Se $_3$ and its favourable interface with graphene for charge extraction. Further research into device design, mechanisms and fabrication are crucial for reliable, optimized and predictable memristive behaviours and

graphene-based vdW heterostructures with ferroelectric tunnelling barriers. Also, the development of ferroelectric semiconductors with controlled n - and p -type doping is critical to future implementation of ferroelectrics in multi-functional devices.

4. Experimental section

Materials and device fabrication The α -In $_2$ Se $_3$ crystals were grown using the Bridgman method from a polycrystalline melt of In and Se with atomic ratio of 40:60. The crystal structure of the α -In $_2$ Se $_3$ single crystals was studied by x-ray diffraction using a DRON-3M diffractometer. The crystals exhibit either a rhombohedral (3R) or a hexagonal (2H) crystal structure. Here we focus on the hexagonal (2H) phase with lattice parameters $a = b = 4.031 \pm 0.003$ Å and $c = 19.210 \pm 0.009$ Å. For the rhombohedral (3R) phase, $a = b = 4.017 \pm 0.003$ Å and $c = 28.870 \pm 0.009$ Å. Raman spectroscopy and imaging studies on flakes and bulk crystals reveal the characteristic vibrational modes of 2H α -In $_2$ Se $_3$, providing a means to distinguish it from other phases (figure S1 in the supplementary materials). The PL emission of bulk α -In $_2$ Se $_3$ is centred at about 1.4 eV at 300 K and blue-shifts with decreasing layer thickness. In its bulk form, α -In $_2$ Se $_3$ contains native donors. Hall effect measurements on bulk α -In $_2$ Se $_3$ at $T = 300$ K indicate an electron density $n = 4.9 \times 10^{17}$ cm $^{-3}$ and an electron mobility in the layer plane of $\mu = 405$ cm 2 V $^{-1}$ s $^{-1}$. The relatively high electron density arises from impurities residing in the interlayer spaces. These limit the OOP mobility, which is 50 times smaller (8 cm 2 V $^{-1}$ s $^{-1}$) than in the layer plane [26]. Figure 1(a) in the main text shows a schematic illustration of our

devices. These graphene/ α -In₂Se₃/graphene heterostructures are assembled onto a SiO₂/*p*-Si substrate (SiO₂ layer thickness of 300 nm) using chemical vapour deposition (CVD) graphene and α -In₂Se₃ flakes. For the stamping of top and bottom graphene, we use a needle-assisted transfer process of patterned graphene microsheets, as described in [40]. The top and bottom graphene flakes are deposited sequentially onto prepared metal contacts (Au/Ti (100 nm/10 nm)) using a dry transfer method under ambient conditions. Flakes of α -In₂Se₃ are exfoliated onto polydimethylsiloxane (PDMS) from a low-tack, low-residue tape and identified using transmission and reflection mode optical microscopy. Then, using a micromanipulator stage, an exfoliated flake of α -In₂Se₃ on PDMS is aligned to the predeposited bottom graphene flake and brought into contact. The PDMS is then slowly retracted in order to deposit α -In₂Se₃. Finally, the top graphene contact is aligned to the α -In₂Se₃ and Au/Ti metal contact.

Optical, electrical and microscopy studies Images of the layers' topography were acquired by atomic force microscopy (MFP3D) in non-contact mode under ambient conditions.

Local reversible polarisation of ferroelectric domains [41] and PFM maps of α -In₂Se₃ films were conducted using a commercial scanning probe microscope (Multimode with Nanoscope-V controller, Bruker, USA) in ambient atmosphere using small contact radius conductive tips (PtSi-CONT, Nanosensors, Switzerland) in both resonance and non-resonance contact mode [42]. Transport measurements in the dark and under light illumination were conducted in vacuum (2×10^{-6} mbar). All experiments were conducted with the bottom-graphene electrode grounded. The experimental setup for the micro-Raman and micro-PL spectroscopy studies at room temperature comprises a He-Ne laser ($\lambda = 633$ nm), an *x-y-z* motorized stage and an optical confocal microscope system equipped with a 0.5 m long monochromator with 1200 g mm^{-1} and 150 g mm^{-1} gratings. The laser beam was focused to a diameter $d \sim 1 \mu\text{m}$ using a $50\times$ objective. The signal was detected by a Si-charge-coupled device camera. The optical studies were performed at low excitation power to avoid excessive heating. The temporal dynamics of the photocurrent was investigated under constant bias voltage and illumination by a mechanically modulated He-Ne laser with $\lambda = 633$ nm and frequency $f < 200$ Hz. The photocurrent signal was measured using a Tektronix DPO 4032 digital oscilloscope and a Keithley2400 was used as a DC voltage source. For the time-resolved measurements of the current, the device was connected in series with a 1 M Ω resistor and the voltage on the 1 M Ω resistor recorded using the oscilloscope with a low-noise level.

Data availability statement

The data that support the findings of this study are available upon reasonable request from the authors.

Acknowledgments

This project has received funding from the European Union's Horizon 2020 research and innovation programme under Grant Agreement Graphene Core3. This work was also supported by the Engineering and Physical Sciences Research Council (Grant No. EP/M012700/1).

Conflict of interest

The authors declare that they have no competing financial interests.

Author contributions

S X and A P designed the experiments; Z R K and Z D K grew the In₂Se₃ crystals; S X, Z R K and N B fabricated the exfoliated layers and devices; S X led the experiments with the support of A D, O M, A P and K W; E C, O K and W Y conducted the domain switching and PFM studies; S X and A P co-wrote the paper; all authors took part in the discussion and analysis of the data.

ORCID iDs

Shihong Xie  <https://orcid.org/0000-0003-1469-7788>

Zakhar R Kudrynskiy  <https://orcid.org/0000-0003-3983-9316>

Nilanthy Balakrishnan  <https://orcid.org/0000-0002-7236-5477>

Oleg Kolosov  <https://orcid.org/0000-0003-3278-9643>

Kaiyou Wang  <https://orcid.org/0000-0002-6017-7575>

Amalia Patanè  <https://orcid.org/0000-0003-3015-9496>

References

- [1] Valasek J 1921 Piezo-electric and allied phenomena in Rochelle salt *Phys. Rev.* **17** 475–81
- [2] Scott J F 2007 Applications of modern ferroelectrics *Science* **315** 954–9
- [3] Bhalla A S and Saxena A 2020 Ferroelectricity: 100 years on *Phys. World* **33** 38–41
- [4] 2020 A century of ferroelectricity *Nat. Mater.* **19** 129
- [5] Belianinov A, He Q, Dziaugys A, Maksymovych P, Eliseev E, Borisevich A, Morozovska A, Banys J, Vysochanskii Y and Kalinin S V 2015 CuInP₂S₆ room temperature layered ferroelectric *Nano Lett.* **15** 3808–14

- [6] Xue F *et al* 2018 Room-temperature ferroelectricity in hexagonally layered α -In₂Se₃ nanoflakes down to the monolayer limit *Adv. Funct. Mater.* **28** 1803738
- [7] Poh S M *et al* 2018 Molecular beam epitaxy of two-dimensional In₂Se₃ and its giant electroresistance switching in ferroresistive memory junction *Nano Lett.* **18** 6340–6
- [8] Xue F *et al* 2018 Multidirection piezoelectricity in mono- and multilayered hexagonal α -In₂Se₃ *ACS Nano* **12** 4976–83
- [9] Wan S *et al* 2019 Nonvolatile ferroelectric memory effect in ultrathin α -In₂Se₃ *Adv. Funct. Mater.* **29** 1808606
- [10] Wang L, Wang X, Zhang Y, Li R, Ma T, Leng K, Chen Z, Abdelwahab I and Loh K P 2020 Exploring ferroelectric switching in α -In₂Se₃ for neuromorphic computing *Adv. Funct. Mater.* **30** 2004609
- [11] Xue F *et al* 2020 Optoelectronic ferroelectric domain-wall memories made from a single van der Waals ferroelectric *Adv. Funct. Mater.* **30** 2004206
- [12] Si M *et al* 2019 A ferroelectric semiconductor field-effect transistor *Nat. Electron.* **2** 580–6
- [13] Yang J J, Strukov D B and Stewart D R 2013 Memristive devices for computing *Nat. Nanotechnol.* **8** 13–24
- [14] Ahn C H, Rabe K M and Triscone J-M 2004 Ferroelectricity at the nanoscale: local polarization in oxide thin films and heterostructures *Science* **303** 488–91
- [15] Ding W, Zhu J, Wang Z, Gao Y, Xiao D, Gu Y, Zhang Z and Zhu W 2017 Prediction of intrinsic two-dimensional ferroelectrics in In₂Se₃ and other III₂-VI₃ van der Waals materials *Nat. Commun.* **8** 14956
- [16] Hou P, Xing S, Liu X, Chen C, Zhong X, Wang J and Ouyang X 2019 Resistive switching behavior in α -In₂Se₃ nanoflakes modulated by ferroelectric polarization and interface defects *RSC Adv.* **9** 30565–9
- [17] Choi M S, Cheong B-K, Ra C H, Lee S, Bae J-H, Lee S, Lee G-D, Yang C-W, Hone J and Yoo W J 2017 Electrically driven reversible phase changes in layered In₂Se₃ crystalline film *Adv. Mater.* **29** 1703568
- [18] Xiao J *et al* 2018 Intrinsic two-dimensional ferroelectricity with dipole locking *Phys. Rev. Lett.* **120** 227601
- [19] Cui C *et al* 2018 Intercorrelated in-plane and out-of-plane ferroelectricity in ultrathin two-dimensional layered semiconductor In₂Se₃ *Nano Lett.* **18** 1253–8
- [20] Wan S, Li Y, Li W, Mao X, Zhu W and Zeng H 2018 Room-temperature ferroelectricity and a switchable diode effect in two-dimensional α -In₂Se₃ thin layers *Nanoscale* **10** 14885–92
- [21] Xue F *et al* 2019 Gate-tunable and multidirection-switchable memristive phenomena in a van der Waals ferroelectric *Adv. Mater.* **31** 1901300
- [22] Wang X *et al* 2021 Van der Waals engineering of ferroelectric heterostructures for long-retention memory *Nat Commun.* **12** 1109
- [23] Küpers M, Konze P M, Meledin A, Mayer J, Englert U, Wuttig M and Dronskowski R 2018 Controlled crystal growth of indium selenide, In₂Se₃, and the crystal structures of α -In₂Se₃ *Inorg. Chem.* **57** 11775–81
- [24] Sze S M 2008 *Semiconductor Devices: Physics and Technology* (New York: Wiley)
- [25] Lang D V 1974 Deep-level transient spectroscopy: a new method to characterize traps in semiconductors *J. Appl. Phys.* **45** 3023–32
- [26] Zasloukin A V, Kovalyuk Z D and Mintyanski I V 2007 Electrical properties of In₂Se₃ layered crystals doped with cadmium, iodine, or copper *Inorg. Mater.* **43** 1271–4
- [27] Grinberg I *et al* 2013 Perovskite oxides for visible-light-absorbing ferroelectric and photovoltaic materials *Nature* **503** 509–12
- [28] Yuan Y, Xiao Z, Yang B and Huang J 2014 Arising applications of ferroelectric materials in photovoltaic devices *J. Mater. Chem. A* **2** 6027–41
- [29] Lee D, Baek S H, Kim T H, Yoon J-G, Folkman C M, Eom C B and Noh T W 2011 Polarity control of carrier injection at ferroelectric/metal interfaces for electrically switchable diode and photovoltaic effects *Phys. Rev. B* **84** 125305
- [30] Xu K, Jiang W, Gao X, Zhao Z, Low T and Zhu W 2020 Optical control of ferroelectric switching and multifunctional devices based on van der Waals ferroelectric semiconductors *Nanoscale* **12** 23488–96
- [31] Lv Q, Yan F, Wei X and Wang K 2018 High-performance, self-driven photodetector based on graphene sandwiched GaSe/WS₂ heterojunction *Adv. Opt. Mater.* **6** 1700490
- [32] Balakrishnan N *et al* 2016 Quantum confinement and photoresponsivity of β -In₂Se₃ nanosheets grown by physical vapour transport *2D Mater.* **3** 025030
- [33] Buscema M, Groenendijk D J, Blanter S I, Steele G A, van der Zant H S J and Castellanos-Gomez A 2014 Fast and broadband photoresponse of few-layer black phosphorus field-effect transistors *Nano Lett.* **14** 3347–52
- [34] Mudd G W *et al* 2013 High broad-band photoresponsivity of mechanically formed InSe-graphene van der Waals heterostructures *Adv. Mater.* **27** 3760–6
- [35] Yan F *et al* 2017 Fast, multicolor photodetection with graphene-contacted p-GaSe/n-InSe van der Waals heterostructures *Nanotechnology* **28** 27LT01
- [36] Jacobs-Gedrim R B *et al* 2014 Extraordinary photoresponse in two-dimensional In₂Se₃ nanosheets *ACS Nano* **8** 514–21
- [37] Wu G *et al* 2016 Visible to short wavelength infrared In₂Se₃-nanoflake photodetector gated by a ferroelectric polymer *Nanotechnology* **27** 364002
- [38] Island J O, Blanter S I, Buscema M, van der Zant H S J and Castellanos-Gomez A 2015 Gate controlled photocurrent generation mechanisms in high-gain In₂Se₃ phototransistors *Nano Lett.* **15** 7853–8
- [39] Li W, Dai M, Hu Y, Chen H, Zhu X, Yang Q and Hu P 2019 Synchronous enhancement for responsivity and response speed in In₂Se₃ photodetector modulated by piezoresistive effect *ACS Appl. Mater. Interfaces* **11** 47098–105
- [40] Bie Y-Q *et al* 2011 Site-specific transfer-printing of individual graphene microscale patterns to arbitrary surfaces *Adv. Mater.* **23** 3938–43
- [41] Kolosov O, Gruverman A, Hatano J, Takahashi K and Tokumoto H 1995 Nanoscale visualization and control of ferroelectric domains by atomic force microscopy *Phys. Rev. Lett.* **74** 4309–12
- [42] Stephen J, Baddorf A P and Kalinin S V 2006 Dynamic behaviour in piezoresponse force microscopy *Nanotechnology* **17** 1615–28